United States Department of Commerce
Technology Administration
National Institute of Standards and Technology

NISTIR 5062

Relative Permittivity Measurement of Rectangular Copper-Laminated Substrates Using the Full-Sheet Resonance Technique

Richard L. Lewis

NISTIR 5062

Relative Permittivity Measurement of Rectangular Copper-Laminated Substrates Using the Full-Sheet Resonance Technique

Richard L. Lewis

Electromagnetic Fields Division
Electronics and Electrical Engineering Laboratory
National Institute of Standards and Technology
Boulder, Colorado 80303-3328

April 1997

U.S. DEPARTMENT OF COMMERCE, William M. Daley, Secretary
TECHNOLOGY ADMINISTRATION, Mary L. Good, Under Secretary for Technology
NATIONAL INSTITUTE OF STANDARDS AND TECHNOLOGY, Robert E. Hebner, Acting Director

Relative Permittivity Measurement of Rectangular Copper-Laminated Substrates Using the Full-Sheet Resonance Technique

Richard L. Lewis

Electromagnetic Fields Division
National Institute of Standards and Technology
Boulder, Colorado 80303-3328

A measurement program has been undertaken at NIST to evaluate the full-sheet resonance (FSR) technique, from which consistent relative permittivity values have been obtained. We present an analysis of the theory underlying the FSR technique, along with a theoretical formulation correcting full two-port scattering-matrix measurements of a resonant cavity for the effects of coupling between the external measurement circuit and the cavity. A circuit analysis modeling the resonant cavity and its external circuit is presented, along with a least-squares solution for the resonant cavity's primary resonance parameters. The least-squares analysis features a slight rearrangement of an earlier formulation leading to a more numerically stable solution. An even earlier solution for a resonant cavity's unloaded quality factor, also using a least-squares solution to obtain a coupling correction, is presented for comparison. The application of these coupling correction formulations to the FSR technique is discussed, and results from these two correction formulations are compared with uncorrected results for two sample FSR panels. Computed least-squares data-scatter uncertainties are obtained for each FSR permittivity measurement, which are then used to obtain overall uncertainty estimates for each panel's measured permittivity, including a repeatability uncertainty estimate. These overall uncertainty estimates are compared to our earlier uncorrected FSR uncertainty estimate, showing a tightening of the uncertainty interval for corrected measurements. Finally, our measured FSR permittivities are compared with re-entrant cavity substrate permittivity measurements, showing agreement within expected uncertainty limits between the two techniques.

Key words: coupling correction; dielectric constant; FSR; full-sheet resonance; least-squares analysis; relative permittivity; uncertainty analysis

1. Introduction

A number of authors have described a convenient method for measuring the relative permittivity of dielectric substrates having copper-clad top and bottom surfaces [1-5]. This

method, known as the full-sheet resonance (FSR) technique for measuring microwave circuit board substrates, determines the dielectric substrate's relative permittivity ϵ'_r by measuring the resonant frequencies of the resulting parallel plate cavity. Nondestructive measurement techniques such as FSR are important to the microwave communications industry where knowledge of substrate permittivity is critical to maintaining competitiveness. The technique is independent of substrate thickness, but is not capable of evaluating the uniformity of the relative permittivity over the substrate. A measurement program has been undertaken at NIST to evaluate the FSR technique using an automatic network analyzer (ANA), and results to date demonstrate that consistent values for the relative permittivity are obtained. Here, an improved formulation for carrying out FSR permittivity calculations is presented, along with a formulation for correcting resonant cavity measurements for the effects of coupling. Details on improved FSR panel coupling are also presented, along with associated measurement uncertainties.

2. Measurement Configuration

Primarily, thin dielectric substrates having open sides and copper-clad top and bottom surfaces were tested. The entire panel acts as a resonant cavity, so by measuring the panel's resonant frequencies we obtain the average relative permittivity of the substrate. Since multiple resonant modes occur within the cavity, construction of a mode table is necessary to identify the particular mode excited at a given resonant frequency, which in turn requires keeping an accurate count of the resonant excitation frequencies encountered. The presence of closely spaced modes increases the difficulty of maintaining an accurate resonant frequency count. Consequently, although the number of possible resonant modes within a panel is limitless, only the lower order modes are useful for determining relative permittivity. Since accurate permittivity measurements are limited to the panel's low-order resonant frequencies, higher frequency measurements require reducing the size of the panel.

We described results obtained using weak coupling between the ANA and square FSR panels in our earlier report [6]. In the present study, rectangular FSR panels are strongly coupled to the ANA, as shown in Figure 1, using two APC-7 7mm precision coaxial connectors positioned at opposite corners of the panel. Coupling between the coaxial connectors and the FSR panel needs to be optimized to maintain an accurate count of the resonances excited within the panel. This was partially accomplished by turning the coaxial connectors so they directly faced each other. In our earlier work [6], weak coupling just sufficient for the measurement was achieved by maintaining direct contact between one coaxial connector's center conductor and the panel's upper copper sheet and direct contact between the inside of the opposing coaxial connector's outer conductor and the panel's lower copper sheet. FSR panel resonances were observed by measuring frequencies at which the transmission scattering-matrix coefficient S_{12} peaked. Strong coupling, allowing full scattering-matrix observation of the resonances by measuring both reflection and transmission coefficients, was achieved by inserting both corners of the FSR panel far enough into the coaxial connector openings to maintain direct contact between the coaxial-connector's center conductor and the FSR panel's upper copper surface, and direct contact between the inside of the coaxial connector's outer conductor and the FSR panel's lower copper surface.

Inasmuch as the tendency of the FSR panel is to spring back from such direct contact, rubber bands were used to provide light tension drawing the FSR panel corners into the coaxial connector's openings. Caution was needed to prevent the connection between the FSR panel and the coaxial connectors from becoming so taut that the rectangular panel became bowed or warped, causing the observed resonant frequencies to shift. In order to detect any unintended resonant frequency shifts, the expected resonant frequencies were checked against prior measurements made using weak coupling as described above.

The advantage of full scattering-matrix measurement of FSR panel resonances is that it allows either transmission or reflection coefficient measurements to be selected, whichever is most appropriate. Measurements carried out on two sample panels showed reflection coefficient measurements to be less affected by frequency pulling due to the proximity of adjacent resonances than transmission coefficient measurements. Obviously, full scattering-matrix measurements will generally be more accurate than just transmission measurements. The only disadvantage of full scattering-matrix measurements is that strong coupling is generally required; this necessitates correcting the measured results for the effects of coupling to the FSR panels. The next section presents an underlying theoretical analysis of factors other than coupling which affect FSR permittivity measurements, while succeeding sections present a formulation for correcting resonant cavity measurements for the effects of coupling. These corrections are carried out by measuring the amplitude and phase of the scattering-matrix elements over a range of frequencies in the vicinity of the resonance, which in turn requires calibrating the ANA, the price for obtaining accurate FSR permittivities.

3. Theoretical Considerations for Determining FSR Permittivity

The relative permittivity of the substrate in a rectangular FSR panel is obtained from the resonant frequencies of an ideal cavity having perfectly conducting electric walls above and below the dielectric substrate and perfect magnetic walls along the sides [1]. This gives the expression

$$\epsilon_r' = \left(\frac{\pi c}{\omega_{mn}}\right)^2 \left[\left(\frac{m}{x_1}\right)^2 + \left(\frac{n}{y_1}\right)^2\right] , \qquad (1)$$

where c is the speed of light, x_1 and y_1 are the length and width of the panel, m and n are integer-value mode numbers, and ω_{mn} is the radian resonant frequency of an ideal cavity corresponding to the $m \times n^{\text{th}}$ TM_{mn0} mode (electric field vector perpendicular to the conducting plates).

In practice, the resonant frequencies of a real cavity differ from their ideal values due to conductivity and radiation losses, electric or magnetic field perturbation at the cavity coupling points [3], and to overcoupled dual resonant modes [7]. When the FSR panel's side aspect ratio is nearly (but not exactly) equal to the square root of the ratio of two integers, then some modes can have their resonant peaks widened, skewed, or doubled [5]. Also, closely spaced resonances can have their resonant peaks distorted [5] by smearing. Resonances such as these may be used for mode counting but are not useful otherwise. However, if the FSR panel shape is not a square then an unambiguous low order mode can be chosen [4 (fig. 3)] for FSR permittivity measurement.

In the case of a totally closed cavity with imperfectly conducting walls, Collin [8] formulated a correction to such a cavity's ideal resonant frequency using a modal-series expansion, where each mode in the series corresponds to an eigenvalue solution for the field that would exist in a cavity with perfectly conducting walls on all sides. Collin [8] further noted that a cavity having a combination of perfect electric and perfect magnetic walls could be modeled using modal fields appropriate to a mixed boundary condition. Following Collin's [8] analysis for a completely closed cavity, the following expression can be obtained correcting the open-sided FSR cavity for the effects of frequency pulling due to both finite wall conductivity and radiation loss from the open sides.

$$\omega_{mn} = \left[1 + \frac{1}{Q_C} + \frac{B_R/G_R}{Q_R}\right]^{\frac{1}{2}} \omega_0 \ , \tag{2}$$

where Q_C is the open cavity's conductivity quality factor for the metalized sides, Q_R the radiation quality factor [8], $G_R + jB_R \equiv Y_R$ the normalized aperture admittance at the open side walls of the cavity, and ω_0 the cavity's unloaded resonant frequency. As Q_R approaches infinity, corresponding to negligible radiation loss, eq (2) becomes identical with the correction formula obtained by Collin [6]. The derivation of eq (2) readily follows from Collin's formulation [8 (section 7.7 through section 7.9)] by replacing Collin's pure "short-circuit" modes with hybrid "short-circuit open-circuit" modes.

Based on an analysis of a wave reflected from the end of a parallel plate waveguide assuming an extended dielectric slab [9], we expect the aperture susceptance of the open side wall of the cavity to be capacitive. Consequently, B_R will be positive and, in the case of separation distances much less than a tenth of a wavelength between the top and bottom conducting sheets, we expect [10] $B_R/G_R \geq 1$. Moreover, the magnitude of the reflection coefficient from the end of a dielectric-free parallel-plate waveguide [10] is $|\Gamma| = e^{-kt/2}$, where t is the guide width and $k = 2\pi/\lambda$. For typical panel thickness and frequencies under investigation, this would make $|\Gamma|$ close to unity, the character of a fairly good magnetic wall. Also, with a dielectric substrate, the electric field will concentrate within the dielectric, making the aperture an even better magnetic wall.

A theoretical formulation for the conductivity quality factor of a rectangular FSR is given by Taber [11], who obtained

$$Q_C = \frac{\mu_0 \omega t}{2R_s} \ , \tag{3}$$

where μ_0 is free-space permeability, ω is the radian frequency, t is the thickness of the dielectric substrate, and R_s is the surface resistance (including surface roughness [12]) of the metalized sides. Equation (3) shows that Q_C is proportional to t, whereas Q_R is inversely proportional to t [11].

The unloaded quality factor Q_0 of a resonant cavity is obtained [13] by combining the cavity's conductivity, radiation, and dielectric quality factors, resulting in $1/Q_0 = 1/Q_C + 1/Q_R + tan\,\delta$. Consequently, we can eliminate Q_R from eq (2) to obtain

$$\omega_{mn} = \left[1 + \frac{1}{Q_0} + \left(\frac{B_R}{G_R} - 1\right)\left(\frac{1}{Q_0} - \frac{1}{Q_C}\right) - \frac{B_R}{G_R}\tan\delta\right]^{\frac{1}{2}} \omega_0 \ . \tag{4}$$

To a first approximation, the ratio B_R/G_R can be estimated using a theoretical formulation [9] corresponding to the simpler case of an extended dielectric slab, although a theoretical analysis similar to earlier work [10, 14] for the case where the dielectric substrate terminates at the end of the guide would be preferable since this would match the FSR configuration under study. Such an analysis should also produce a theoretical value for Q_R (for instance, an expression for Q_R is given in reference [15] for a circular disk). Determining Q_R theoretically would result in an ability to compute the dielectric loss tangent $tan\,\delta = 1/Q_0 - 1/Q_C - 1/Q_R$. Measured FSR unloaded quality factors are typically around 100 with relative uncertainties greater than 3%; consequently the relative uncertainty in computing $tan\,\delta$ could be around $\pm 5\%$ if the substrate's loss tangent is around 10^{-2} and around $\pm 50\%$ if the loss tangent is around 10^{-3}.

In addition to resonant frequency pulling, electric-field fringing beyond the dielectric substrate can lower the measured relative permittivity. This systematic error can be corrected by multiplying the right side of eq (1) by the idealized parallel-plate capacitance $\epsilon'_r(C+C_f)$ and dividing by the actual capacitance $\epsilon'_r C + C_f$, where $C = \epsilon_0\,(x_1 y_1/t)$, ϵ_0 is free-space permittivity, and C_f is the fringing capacitance of the panel. The relative permittivity is then obtained iteratively using

$$\dot{\epsilon}'_r = \frac{C + C_f}{C + C_f/\epsilon'_r} \left(\frac{\pi\, c}{\omega_{mn}}\right)^2 \left[\left(\frac{m}{x_1}\right)^2 + \left(\frac{n}{y_1}\right)^2\right] , \tag{5}$$

where $\dot{\epsilon}'_r$ is an improved value for the permittivity and the initial value ϵ'_r is obtained from eq (1). Assigning a value to C_f is problematical, although as an approximation Kirchhoff's formula [16] for the fringe capacitance of two parallel circular disks could be used.

4. Equivalent Circuit Model of a Resonant Cavity

An ANA may be used to measure a cavity's loaded resonant frequency and loaded quality factor, from which the cavity's unloaded resonant frequency and unloaded quality factor [17] can be determined. Following Kajfez's analysis [18,19] of a single-port resonant cavity, the equivalent circuit diagram for a two-port resonant cavity in the vicinity of a single isolated resonance is shown in figure 2. The resonant cavity is represented by the parallel circuit elements having primary resonance parameters denoted as ω_0 and Q_0, with energy loss in the cavity modeled by the parallel resistor R_0. The input/output ports of the ANA are represented by the two resistors labeled R_c located at opposite sides of the circuit diagram. These two ANA ports are each connected to a transmission line of characteristic impedance R_c, which in turn are connected to the resonant cavity through the self impedances of the resonant cavity's coupling ports $Z_S = R_S + jX_S$ and $\hat{Z}_S = \hat{R}_S + j\hat{X}_S$. The series reactances X_S and $\hat{X}_S$ are assumed to vary slowly with frequency compared to the resonance under study. A straightforward circuit analysis [19] expresses the S_{11} reflection coefficient, at the input port to the resonant cavity, in terms of the exciting radian frequency ω as

$$S_{11} = \Gamma_d + \frac{d_1 e^{-i\gamma_1}}{1 + i\,Q_\ell \frac{\omega^2 - \omega_\ell^2}{\omega\,\omega_\ell}} . \tag{7}$$

Here, ω_ℓ is the resonant circuit's loaded resonant frequency, Q_ℓ is the resonant circuit's loaded quality factor, and Γ_d is the detuned reflection coefficient corresponding to the coupling port's self impedance such that

$$\frac{X_S}{R_c} = \mathrm{Im}\left(\frac{1+\Gamma_d}{1-\Gamma_d}\right) \ . \tag{8}$$

Moreover,

$$d_1 = \frac{2\,\kappa_1}{1+\kappa} \ , \tag{9}$$

$$\gamma_1 = 2\,\tan^{-1}\left[\frac{X_S/R_c}{\beta}\right] \ . \tag{10}$$

Here, κ_1 is the ratio of the transmission line conductivity (as viewed from the resonant circuit's port) to the resonant circuit's conductivity. An explicit expression [19] for κ_1 in terms of the lumped circuit elements in figure 2 is

$$\kappa_1 = \frac{R_c\,R_0}{(R_c+R_S)^2 + X_S^2} \ . \tag{11}$$

Equation (10) contains $\beta = 1 + R_S/R_c$, while eq (9) introduces κ, the resonant cavity's overall coupling coefficient,

$$\kappa = \beta\,\kappa_1 + \hat{\beta}\,\hat{\kappa}_1 \ . \tag{12}$$

Here, β and κ_1 correspond to the S_{11} port while $\hat{\beta}$ and $\hat{\kappa}_1$ correspond to the S_{22} port. The overall coupling coefficient κ relates the loaded quality factor to an intermediate unloaded quality factor $\widehat{Q}_0$ according to

$$\widehat{Q}_0 = (1+\kappa)\ Q_\ell \ . \tag{13}$$

The unloaded resonant frequency is given by

$$\omega_0 = \omega_\ell \sqrt{1 - \frac{\kappa_1\,X_S}{\widehat{Q}_0\,R_c} - \frac{\hat{\kappa}_1\,\hat{X}_S}{\widehat{Q}_0\,R_c}} \ . \tag{14}$$

Again, X_S is the S_{11} coupling port's self reactance while $\hat{X}_S$ is the S_{22} coupling port's self reactance. The overall unloaded quality factor of the resonant cavity is obtained with the help of eq (14) as

$$Q_0 = \frac{\omega_0}{\omega_\ell}\,\widehat{Q}_0 = (1+\kappa)\,\frac{\omega_0}{\omega_\ell}\,Q_\ell \ . \tag{15}$$

The transmission component S_{21} of the scattering matrix is readily obtained as

$$S_{21} = \frac{d_3 e^{-i\gamma_3}}{1 + i\,Q_\ell \frac{\omega^2-\omega_\ell^2}{\omega\,\omega_\ell}} \ . \tag{16}$$

where

$$d_3 = \frac{2\sqrt{\kappa_1\,\hat{\kappa}_1}}{1+\kappa} \ . \tag{17}$$

Equations (16) and (17) agree with an earlier expression [20] for the amplitude squared of S_{21}. The phase term in eq (16) is

$$\gamma_3 = \tan^{-1}\left[\frac{X_S/R_c}{\beta}\right] + \tan^{-1}\left[\frac{\hat{X}_S/R_c}{\hat{\beta}}\right] \ . \tag{18}$$

5. Least-Squares Circle Fit to the Equivalent Circuit Model

The preceding section gives a circuit model analysis of a resonant cavity's scattering matrix in the vicinity of an isolated resonance as a function of frequency. The locus of points traced out on a Smith chart by either of the scattering matrix components S_{11} or S_{21}, as given by eqs (7) and (16), is a circle [13]. Kajfez [19] describes a linear least-squares solution for three unknowns which fits measured reflection coefficient data to a circle. However, a slight rearrangement of Kajfez's formulation was required to make his least-squares solution numerically stable. The resulting linear equation for least-squares resolution is

$$z\,S_{11} = \alpha_1 + z\,\alpha_2 - S_{11}\,\alpha_3 \ , \tag{19}$$

where $\alpha_j\,;\ j = 1, 2, 3$ denotes the unknowns to be determined by the least-squares fitting procedure [19]. Specifically, the unknowns are determined by solving the least-squares matrix equation,

$$\begin{bmatrix} \langle 1 \rangle & \langle z \rangle & \langle -S_{11} \rangle \\ \langle -z \rangle & \langle -z^2 \rangle & \langle z\,S_{11} \rangle \\ \langle -S_{11}^* \rangle & \langle -z\,S_{11}^* \rangle & \langle |S_{11}|^2 \rangle \end{bmatrix} \begin{bmatrix} \alpha_1 \\ \alpha_2 \\ \alpha_3 \end{bmatrix} = \begin{bmatrix} \langle z\,S_{11} \rangle \\ \langle -z^2\,S_{11} \rangle \\ \langle -z\,|S_{11}|^2 \rangle \end{bmatrix} \ . \tag{20}$$

Here, $\langle x \rangle \equiv \sum_{i=1}^{N} \{p_i x_i\}$ denotes a weighted sum of N measured components x_i where the weighting coefficients p_i are inversely proportional to a particular measurement's estimated variance [19] and the asterisk denotes a complex conjugate. In eq (19), the S_{11} are measured reflection coefficient data corresponding to a specific complex measurement-frequency difference z, which is defined as

$$z \equiv i\,\frac{\omega^2 - \tilde{\omega}_\ell^{\,2}}{\omega\tilde{\omega}_\ell} \ . \tag{21}$$

Here, ω is the measured radian frequency and $\tilde{\omega}_\ell$ is the (unknown) loaded resonant frequency. An initial value for $\tilde{\omega}_\ell$ is obtained from the measured resonant minimum; then an iterative procedure [19] is used to obtain a refined value for $\tilde{\omega}_\ell$ by solving eq (19) for the S_{11} reflection coefficient's resonance minimum, resulting in $z = \frac{1}{2}(\alpha_3^* - \alpha_3)$. Using this result with eq (21) produces the iterated value, $\tilde{\omega}_\ell = \hat{\tilde{\omega}}_\ell\,[-\frac{i}{4}(\alpha_3^* - \alpha_3) + \sqrt{1 - \frac{1}{16}(\alpha_3^* - \alpha_3)^2}\,]$,

where $\hat{\omega}_\ell$ represents the previous value. Kajfez's formulation [19] also produces a least-squares fit data-scatter uncertainty estimate for each of the unknown least-squares fitting coefficients in eq (19).

From eqs (7) and (19) we make [19] the identification $\Gamma_d = \alpha_2$. Also, from eq (7) we see that the Q circle diameter is equal to d_1. Using eq (19) to form the difference $S_{11} - \alpha_2$, we find the difference's maximum amplitude (the minimum of S_{11}) occurs at the resonance minimum $z = \frac{1}{2}(\alpha_3^* - \alpha_3)$ [19], while the difference's minimum amplitude occurs as z approaches infinity. Consequently, the resulting expression for the numerator in eq (7), similar to Kajfez's [19] original expression, is given by

$$d_1 \, e^{-i\gamma_1} = 2 \, \frac{\alpha_1 - \alpha_2 \, \alpha_3}{\alpha_3 + \alpha_3^*} \quad . \tag{22}$$

With this result we can solve eqs (7) and (19) for the unloaded quality factor, obtaining $Q_\ell = 1/\mathrm{Re}(\alpha_3)$. Moreover, by noting that $\beta = 1 + R_S/R_c$ equals the reciprocal of a constant-resistance circle's radius [21] on a Smith Chart, Kajfez [19] obtains the expression

$$\beta = \frac{2\,(1 - |\Gamma_d| \cos\phi)}{1 - |\Gamma_d|^2} \quad , \tag{23}$$

where

$$\phi = \tan^{-1}\left[\frac{\mathrm{Im}(\Gamma_d - \Gamma_c)}{\mathrm{Re}(\Gamma_d - \Gamma_c)}\right] - \tan^{-1}\left[\frac{\mathrm{Im}(\Gamma_d)}{\mathrm{Re}(\Gamma_d)}\right] \quad . \tag{24}$$

Here, Γ_c denotes the center of the resonance circle. The center's location is obtained [19] from the least-squares fit coefficients as

$$\Gamma_c = \frac{\alpha_1 + \alpha_2 \, \alpha_3^*}{\alpha_3 + \alpha_3^*} \quad , \tag{25}$$

which takes into account the location of the resonance minimum at $z = \frac{1}{2}(\alpha_3^* - \alpha_3)$.

The S_{22} port's Q circle diameter $\hat{d}_1$ can be obtained using an expression analogous to eq (22). Moreover, $\hat{d}_1$ can be expressed in terms of the circuit model similar to eq (9) as $\hat{d}_1 = 2\,\hat{\kappa}_1 \,/\, (1 + \kappa)$. Solving this expression along with eqs (9) and (12) for the overall coupling coefficient κ, we obtain the useful computational expression

$$\kappa = \frac{\beta \, d_1 + \hat{\beta} \, \hat{d}_1}{2 - \beta \, d_1 - \hat{\beta} \, \hat{d}_1} \quad . \tag{26}$$

In addition to the preceding least-squares analysis fitting measured reflection coefficients to a circle, the measured transmission coefficients $S_{12} = S_{21}$ (due to reciprocity) can also be fitted to a circle. In the case of the transmission coefficient's least-squares analysis a two-term linear equation may be used inasmuch as the circle intersects the Smith-chart origin, thus reducing the number of unknowns by one as compared to the reflection coefficient

case. With a two-term linear equation numerical stability of the least-squares procedure is generally assured. A suitable linear least-squares equation for the transmission coefficient measurements is

$$z\, S_{21} = a_1 - S_{21}\, a_3 \ , \tag{27}$$

where the complex measurement-frequency difference z is again expressed by eq (21), except now the initial value of $\tilde{\omega}_\ell$ is obtained from the measured resonant maximum; an iterative procedure similar to that described earlier (using a_3 in place of α_3) is used to obtain a refined value for the loaded resonant frequency.

Taking into account the resonant frequency maximum, $z = \frac{1}{2}(a_3^* - a_3)$, and equating eqs (16) and (27) we find the transmission circle diameter is equal to the magnitude of $d_3\, e^{-i\gamma_3} = 2\, a_1/(a_3 + a_3^*)$, where the phase term's circuit-model representation γ_3 is given by eq (18). Now recomparing eqs (16) and (27) we can make the identification $Q_\ell = 1/\mathrm{Re}(a_3)$.

When a full set of scattering-matrix measurements are taken, the preceding least-squares circuit analyses show that a resonant cavity's loaded resonant frequency and loaded quality factor can either be obtained from transmission coefficient measurements or from reflection coefficient measurements, that the coupling coefficients κ_1 and $\hat{\kappa}_1$ can be obtained a number of different ways using various combinations of results obtained from carrying out least-squares circle fits on measured S_{11}, S_{22}, and $S_{21} = S_{12}$ data using eqs (9) and (17), and that the coupling-port's self reactances can be obtained either from eq (8) or from eqs (10) and (18). When just transmission coefficient measurements are available, then the additional simplifying assumption of lossless symmetrical coupling-port impedances is needed.

6. Determining a Cavity's Primary Resonance Parameters

As previously indicated, any two independent scattering matrix components (recall $S_{12} = S_{21}$) are sufficient to determine a resonant cavity's primary resonance parameters, the unloaded resonant frequency and the unloaded quality factor, provided that the circuit model assumption of a single isolated resonance remains valid. With full scattering-matrix measurement of FSR panels, the transmission-coefficient measurement portion was found to be more prone to adjacent resonance distortion than the reflection-coefficient measurement portion. As a result, calculations using just reflection coefficient data were chosen as the preferred method for determining a FSR panel's primary resonance parameters.

The primary resonance parameters are determined by first completing a circle fit for measured S_{11} and S_{22} reflection coefficient data, during which the quantities d_1, $\hat{d}_1$, β, and $\hat{\beta}$ are determined using eqs (20), (22), and (23). The external series reactances X_S/R_c and $\hat{X}_S/R_c$ are calculated using eq (8), and the overall coupling coefficient κ is evaluated using eq (26). The values used for the loaded quality factor and loaded resonant frequency in eqs (13) and (14) are obtained by averaging corresponding values from the S_{11} and S_{22} least-squares evaluations. The overall unloaded quality factor is then obtained using eq (15), which completes the process of determining the cavity's primary resonance parameters.

In general, the solution for the primary resonance parameters of a cavity having a single isolated resonance is over determined when full scattering-matrix measurements are taken. For the purpose of estimating the consistency of the circuit model's assumption of a single isolated resonance, the cavity's primary resonance parameters are calculated using

both the preferred formulation described above and an alternate formulation which uses transmission-coefficient and reflection-coefficient measurements to determine the cavity's primary resonance parameters. The results from these two independent computations are then compared. When the multiple resonances of a real cavity are well separated from each other, then the results obtained from the preferred formulation described above and the alternate formulation are equivalent, so either formulation could be used to determine the cavity's primary resonance parameters. However, adjacent resonant modes can cause the results computed using these two independent formulations to diverge. Consequently, the difference between the results from these two independent formulations serves to measure the validity of the single resonant mode assumption built into the circuit model.

I will just give a brief description of the alternate formulation's principal aspects. First, a circle fit for all four scattering-matrix components is carried out using eqs (19) and (27). Then, values for d_1 and $\hat{d}_1$ are determined for the alternate formulation, except that now the quantity $d_3 - \sqrt{d_1\,\hat{d}_1}$, which according to eqs (9) and (17) should equal zero, is incorporated
into the result. Equation (23) is again used for β and $\hat{\beta}$, following which an alternate coupling
coefficient κ is obtained from eq (26) using these modified d_1 and $\hat{d}_1$ values. The loaded quality factor and loaded resonant frequency in eqs (13) and (14) are obtained by averaging corresponding values from the S_{12} and S_{21} least-squares evaluations, while the sum of external series reactances in eq (14) follows from eqs (10) and (18) using

$$2\,(\frac{\kappa_1\,X_S}{R_c} + \frac{\hat{\kappa}_1\,\hat{X}_S}{R_c}) = \kappa\,(1 - \tan\frac{\gamma_1}{2}\tan\frac{\hat{\gamma}_1}{2})\tan\gamma_3 + (\beta\,\kappa_1 - \hat{\beta}\,\hat{\kappa}_1)\,(\tan\frac{\gamma_1}{2} - \tan\frac{\hat{\gamma}_1}{2})\,.$$

Here, $\tan\frac{\gamma_1}{2} = -\mathrm{Im}\,w\,/\,(|w| + \mathrm{Re}\,w)$ with $w \equiv d_1\,e^{-i\gamma_1} = 2\,(\alpha_1 - \alpha_2\,\alpha_3)\,/\,(\alpha_3 + \alpha_3^*)$ from eq (22) is used for two of the tangent functions, while $\tan\gamma_3 = -\mathrm{Im}\,u\,/\,\mathrm{Re}\,u$ with $u \equiv 2\,a_1/(a_3 + a_3^*)$. The overall unloaded quality factor again follows from eq (15).

Using Kajfez's formulation [19], a least-squares data-scatter uncertainty estimate is obtained for each unknown fitting coefficient in eq (19). The estimated variance is proportional to the weighted sum of the squared error at each measurement point multiplied by a diagonal element from the matrix inverse of eq (20)'s coefficient matrix [19]. The law of propagation of uncertainty [22] is used to obtain each subsequently derived parameter's combined uncertainty. Component uncertainty estimates are combined using a root sum of squares of individual uncertainties to obtain an overall uncertainty estimate, except for repeatability, for the cavity's primary resonance parameters. The squared difference between the primary resonance parameter's two alternative formulations is included in the root square sum of variances to estimate model consistency.

In addition to the previously described preferred and alternate formulas for the primary resonance parameters, numerical results are presented using an earlier formulation by Estin and Janezic [20] for the unloaded quality factor. The loaded resonant frequency f_ℓ' used in this formulation [20] coincides with the transmission measurement peak (or reflection measurement dip), neglecting any correction for the coupling-port's self impedance on the overall resonant frequency. Estin and Janezic [20] evaluate the cavity's loaded quality

factor Q'_ℓ using a linear least-squares fit to the measured transmission coefficients S_{21}, resulting in the least-squares fitting equation [20]

$$f - f'_\ell = \frac{f'_\ell}{2Q'_\ell}\sqrt{\left|\frac{S_{21_{max}}}{S_{21}}\right|^2 - 1} \ . \tag{28}$$

Here, $|S_{21_{max}}|$ is the maximum value of $|S_{21}|$ and f is the measured frequency. Equation (28) can be obtained from eq (16) by making the approximation, $(\omega^2 - {\omega_\ell}^2)/\omega \approx 2(\omega - \omega_\ell)$. Estin and Janezic [20] also use a least-squares algorithm for fitting a circle to orthogonal (real and imaginary) component data, which is used with measured S_{11} and S_{22} reflection coefficient data to obtain the two circle radii r_1 and $\hat{r}_1$. These two circle radii are then used [20] to obtain an overall coupling coefficient for the two port cavity which neglects iris coupling resistance, resulting in $\kappa' = (r_1 + \hat{r}_1)/(1 - r_1 - \hat{r}_1)$, an expression very similar to eq (26). They then use [20] the standard expression $Q'_0 = (1 + \kappa')\, Q'_\ell$ for the unloaded quality factor.

7. FSR Permittivity Evaluations

A simplified formula for computing FSR permittivity is obtained by neglecting fringing capacitance correction (eq (5)) and retaining just the first term of the ideal resonant frequency correction in eq (4). The result is

$$\epsilon'_r = \left(\frac{\pi\, c}{\omega_0}\right)^2 \frac{(m/x_1)^2 + (n/y_1)^2}{1 + 1/Q_0} \ , \tag{29}$$

where ω_0 and Q_0 are the measured primary resonance parameters. An uncertainty estimate for ϵ'_r is obtained from the law of propagation of uncertainty [22], using previously computed least-squares data-scatter uncertainty estimates for the primary resonance parameters. Since these computations do not take measurement repeatability or other factors such as fringing capacitance or a full treatment of adjacent resonance distortion into account, the results are labeled 'limited' uncertainty estimates.

In addition to determining substrate permittivity using eq (29), an alternative relative permittivity evaluation for $\epsilon'_{r_{(est)}}$ is carried out, corresponding to using Estin and Janezic's formulation [20] for the unloaded quality factor, by replacing ω_0 and Q_0 in eq (29) with the parameters $2\pi f'_\ell$ and Q'_0 obtained as described above. Also, for comparison with our earlier [6] formulation, which used loaded quality factors, a third relative permittivity evaluation is carried out by replacing the primary resonance parameters in eq (29) with $2\pi f'_\ell$, the frequency corresponding to the transmission measurement's peak value, and with $\widetilde{Q}_\ell = f'_\ell\,/(BW)$, where BW denotes the transmission measurement's 3 dB bandwidth [17]. This last expression for FSR permittivity is the same as Howell's [2] original proposal.

8. Presentation of Computed Results

FSR measurements were carried out for two different resonant panels. Each panel had a side aspect ratio approximately equal to $\sqrt{2}$. Tables 1 and 2 present results obtained for FSR panel 1 which had a nominal dielectric thickness of 0.38 mm and side dimensions of 21.54 cm $\times$ 30.48 cm, while tables 3 and 4 present results for FSR panel 2 which

had a nominal dielectric thickness of 1.47 mm and side dimensions of 21.87 cm × 30.88 cm. Nominal permittivity values from re-entrant cavity [23] measurements along with a second independent measurement are also presented for both panels. Tables 2 and 4 present measured quality factors corresponding to the measured permittivities presented in tables 1 and 2. The columns labeled "Measurement Mode" and "Frequency" designate the integral mode numbers and resonant frequency. The columns labeled "Original FSR Tech." present measurement results corresponding to our earlier formulation [6] using loaded quality factors, while the columns labeled "Estin Model" and "Circle Fit FSR" use unloaded quality factors corresponding respectively to Estin and Janezic's [20] and our modified Kajfez [19] formulations as described above. The mathematical symbols in the column headings further relate the quality factor and frequency used in each column's computations to definitions in the text. The columns labeled "Limited Circle Fit Uncert." present computed absolute least-squares uncertainty estimates as described above.

Before each measurement, a full two-port calibration of the ANA was carried out with respect to the precision 7mm coaxial connectors used to couple to each FSR panel. The frequency range that was used with each set of calibrated, full scattering-matrix measurements was just sufficient to encompass the ANA Smith chart's reflection and transmission coefficient circles in the vicinity of the resonance without including frequencies, furthest away from the resonance, beyond which the circles crossed. The frequencies were uniformly stepped over the measurement range with 16 samples averaged per frequency. A subset of the calibrated frequencies was used at each resonance in order to minimize the number of calibrations. Consequently, the number of measurement frequencies at each resonance varied between 50 and 200. Repeating a set of scattering-matrix measurements at a few resonances showed that the number of measurement frequencies was not crucial to these sample resonance's final results.

Due to thin sample thickness, the reentrant cavity uncertainty for sample 1 was about 3% [6], while for sample 2, which was four times as thick, the re-entrant cavity uncertainty was about 1% [24].

In table 2, computed quality factor uncertainty is under 2.5% at the lowest measurement frequency and under 7.5% at the next lowest frequency. However, the percentage difference between quality factors obtained from the two alternative circle-fit computations at these frequencies is 1.5% and 2.4%, respectively. At the next highest frequency in table 2 the computed quality factor uncertainty is 21% due to the proximity of adjacent resonances, although the percentage difference between quality factors from the two alternative circle-fit computations is under 10%. In table 4, the computed quality factor uncertainty at the lowest resonant frequency is 10.5%, while the percentage difference between corresponding alternative quality-factor computations is under 5%. Due to the relatively thick dielectric, only the lowest order mode of panel 2 was unaffected by adjacent-resonance distortion; consequently the resulting computed quality factor uncertainties are greater than 24%. However, except at the next to the lowest resonant frequency, percentage differences between the two alternate quality-factor computations in table 4 is under 4%.

Table 5 presents comprehensive relative uncertainty estimates for FSR permittivity, corresponding to using computed least-squares data-scatter uncertainty estimates in conjunction

with our earlier report's [6] analytical uncertainty analysis. The first column of table 5 presents our earlier report's generic FSR uncertainties [6] for comparison. The next two columns give estimated uncertainties for each specific panel, based on using computed least-squares uncertainties and taking measurement repeatability into account. The combined uncertainty in table 5 is skewed to account for typically lower ϵ_r' values from open-side FSR panel measurements than from other techniques [5], due partly to coupling perturbation [3] and partly to fringing at the open panel sides.

Tables 6 and 7 present results from estimating the conductivity quality factor for each panel using the formula $Q_C = t/\delta_s$, where t denotes substrate thickness and δ_s denotes skin depth (ignoring surface roughness). The unloaded quality factors Q_0 from the modified Kajfez formulation and Q_ℓ' from Estin and Janezic's formulation are reproduced from tables 2 and 4 for comparison convenience. From this, we obtain values for $\tan\delta + 1/Q_R = 1/Q_0 - 1/Q_C$ corresponding to unloaded quality factors from these two different formulations. Unfortunately, no simple interpretation of these results is available since Q_R is a function of the aperture field excited by each resonant mode. However, based on re-entrant cavity loss-tangent measurements, the values in tables 6 and 7 for the sum $\tan\delta + 1/Q_R$ are just slightly larger than the value of $\tan\delta$, showing for the case of tables 6 and 7 that the reciprocal of the radiation quality factor is comparable or slightly smaller than the dielectric loss tangent. This raises the possibility that the FSR technique could be used for approximate loss tangent measurements of lossy dielectrics by developing a reliable theoretical formula to evaluate Q_R for rectangular parallel-plate cavities.

9. Conclusions

Improved expressions for FSR permittivity measurements are presented along with an analytical formulation, based on Kajfez's [19] least-squares circle-fit model, correcting two-port resonant cavity measurements for coupling effects to obtain the cavity's unloaded resonant frequency and unloaded quality factor. A slight rearrangement of Kajfez's [19] formulation improved the numerical stability of the least-squares algorithm used with this technique. The current work presents analytical formulations for obtaining coupling corrections using transmission coefficient and reflection coefficient measurements. Determining a cavity's coupling correction requires the measurement of two independent scattering matrix coefficients, so transmission coefficient measurements alone are insufficient without simplifying assumptions.

Using limited measurements, the FSR technique produced repeatable relative permittivity values which compared favorably to values obtained using other techniques. Improved coupling between coaxial connectors positioned at opposite corners of the FSR panel enabled full scattering-matrix measurement of the panel's resonances to be carried out, producing more accurate FSR measurement results than were obtained previously [6]. Tighter measured-permittivity uncertainty estimates reflect this improvement.

Additional theoretical development is needed to further refine FSR measurement accuracy, which could enable the FSR technique to be used to measure the loss tangents of lossy dielectrics. Improved FSR coupling mechanisms need to be investigated, particularly mechanisms (such as in reference [25]) allowing the panel to be excited along a side rather

than just at a corner. Also, measurement of medium relative permittivity substrates need to be carried out in order to refine the uncertainty analysis.

Helpful comments and discussions with Claude Weil, James Baker-Jarvis, John Grosvenor, Michael Janezic, Chriss Jones, Richard Geyer, and Bill Riddle of the NIST Electromagnetic Properties of Materials project are gratefully acknowledged.

REFERENCES

[1] L. S. Napoli and J. J. Hughes, "A simple technique for the accurate determination of the microwave dielectric constant for microwave integrated circuit substrates," IEEE Trans. Microwave Theory Tech., vol. 19, pp. 664-665, July 1971.

[2] J. Q. Howell, "A quick accurate method to measure the dielectric constant of microwave integrated-circuit substrates," IEEE Trans. Microwave Theory Tech., vol. 21, pp. 142-143, March 1973.

[3] P. H. Ladbrooke, M. H. N. Potok, and E. H. England, "Coupling errors in cavity-resonance measurements on MIC substrates," IEEE Trans. Microwave Theory Tech., vol. 21, pp. 560-562, Aug. 1973.

[4] G. R. Traut, "Modify test fixtures to determine PTFE dielectric constant," Microwaves and RF, vol. 27, pp. 115-124, Feb. 1988.

[5] G. I. Woolaver, "Accurately measure dielectric constant of soft substrates," Microwaves and RF, vol. 29, pp. 153-158, Aug. 1990.

[6] R. L. Lewis, "Relative permittivity measurement of square copper laminated substrates using the full-sheet resonance technique," Natl. Inst. Stand. Technol. NISTIR 5053, 1996.

[7] J. D. Ryder, *Networks, Lines, and Fields*, second ed., Prentice Hall Inc., 1955, pp. 119-133.

[8] R. E. Collin, *Foundations for Microwave Engineering*, second ed., McGraw Hill Inc., 1992, pp. 525-545.

[9] E. F. Kuester, R. T. Johnk, and D. C. Chang, "The thin substrate approximation for reflection from the end of a slab-loaded parallel-plate waveguide with application to microstrip patch antennas," IEEE Trans. Antennas Propagat., vol. 30, no. 5, pp.910-917, Sept. 1982.

[10] L. Lewin, *Advanced Theory of Waveguides*, "Wireless Engineer," Iliffe & Sons, Ltd., 1951, chap. 6.

[11] R. C. Taber, "A parallel plate resonator technique for microwave loss measurements on superconductors," Rev. Sci. Instrum., vol. 61, no. 8, pp. 2200-2206, Aug. 1990.

[12] R. D. Lending, "New criteria for microwave component surfaces," Proc. Nat. Electronics Conf., vol. 11, pp. 391-401, 1955.

[13] D. Kajfez and P. Guillon, ed., *Dielectric Resonators*, Artech House Inc., 1986.

[14] D. C. Chang and E. F. Kuester, "Total and partial reflection from the end of a parallel-plate waveguide with an extended dielectric slab," Radio Sci., vol. 16, no. 1, pp. 1-13, Jan.-Feb. 1981.

[15] A. Fathy, D. Kalokitis, and E. Belohoubek, "Microwave characteristics and characterization of high T_c superconductors," Microwave J., vol. 31, no. 10, p. 75, Oct. 1988.

[16] J. V. L. Parry, "Measurement of permittivity and power factor of dielectrics at frequencies from 300 to 600 Mc/s," Proc. Inst. Elec. Engr., p. III, vol. 98, pp. 303-311, 1951.

[17] E. L. Ginzton, *Microwave Measurements*, McGraw Hill Inc., 1957, pp. 396-409.

[18] D. Kajfez and E. J. Hwan, "Q factor measurement with network analyzer," IEEE Trans. Microwave Theory Tech., vol. 32, no. 7, pp. 666-670, July 1984.

[19] D. Kajfez, *Q Factor*, Vector Fields, Oxford, Miss., 1994.

[20] A. J. Estin and M. D. Janezic, "Improvements in dielectric measurements with a resonant cavity," IEEE Inst. Meas. Conf. Rec., Atlanta, Ga., May 14-16, 1991.

[21] Ramo, Whinnery, and Van Duzer, Fields and Waves in Communication Electronics, 1965.

[22] B. N. Taylor and C. E. Kuyatt, "Guidelines for evaluating and expressing the uncertainty of NIST measurement results," Natl. Inst. Stand. Technol. Tech. Note 1297, Sept. 1994.

[23] J. R. Baker-Jarvis and B. F. Riddle, "Dielectric measurements using a reentrant cavity: mode-matching analysis", Natl. Inst. Stand. Technol. Tech. Note 1384, November 1996.

[24] C. N. Works, "Resonant cavities for dielectric measurements," J. Appl. Phys., vol. 18, pp. 605-612, July 1947.

[25] "Non-destructive full sheet resonance test for permittivity of clad laminates," Inst. for Interconnecting and Packaging Electronic Circuits, IPC-TM-650 Test Methods Manual no. 2.5.5.6, May 1989.

Appendix: **Computer Program Flow Charts**

A computer program for implementing the calculations described in this report has been written in BASIC as a number of modular sub-programs. Here we present a set of three program flow charts to facilitate understanding of the sequence in which calculations are carried out and relating program output to specific mathematical symbols described in the main text.

The main driving program contains a number of softkeys allowing the user to select a desired action, specifically collecting measured data using the ANA, storing data for later retrieval, retrieving stored data, and fitting data to a mathematical circle model. These softkey selections are outlined in flow chart 1. The softkey "NEW DATA MEASURE" requests the user to specify basic parameters for a FSR calculation; then the computer instructs the ANA to read and transfer measured data corresponding to all four S-parameters over the frequency range previously set on the ANA. The softkeys "STORE DATA" and "READ DAT FILE" respectively transfer measured ANA data to mass storage and back again.

Once the softkey labeled "DATA FIT ROUTINES" is selected, the main subprogram "Fit_data" is called, which carries out a Q-circle fit for each of the four measured S parameters; the subprogram then goes on to compute the unloaded quality factor and the unloaded frequency for the resonant cavity, followed by a FSR permittivity calculation using eq (29). Flow chart 2 lists the subroutine calls in the main subprogram "Fit_data," while flow chart 3 lists the subroutine calls carried out by the least-squares data fitting subprograms. Flow charts 2 and 3 list mathematical symbols described in the text indicating specific quantities calculated by a given subroutine. The lack of symbols by a subroutine's name indicates that the subroutine does not carry out computations; for instance, non-computing subroutines might print out previously computed results or initiate a sequence of calls to other subroutines which do carry out computations. All subroutine output are placed in common blocks which other subroutines can access; consequently the data input for a given subroutine is any previously calculated quantity.

An intermediate printout of results follows each least-squares circle fit computation, consisting of all the mathematical symbols that are listed in flow chart 3 above each of the indicated print routines. Computed least-squares data-scatter uncertainty estimates are included in this printout. Following the four scattering-matrix component's least-squares circle-fit calculations shown in flow chart 2, the unloaded quality factor and the unloaded resonant frequency for the cavity are calculated along with a least-squares uncertainty estimate for these primary resonance parameters using the preferred and alternate computation schemes discussed previously. A separate unloaded quality factor calculation is also carried out using Estin and Janezic's formulation [14]. Then two FSR permittivity calculations are carried out using the two different sets of primary resonance parameters that were generated, along with a least-squares uncertainty estimate. Flow chart 2 shows this sequence of events along with a mathematical symbol list for each computational subroutine. The printed output consists of all the mathematical symbols that are listed in flow chart 2 above the routine 'Display_results.'

Figure 1. Coupling schematic between 7 mm coaxial connectors and a copper-clad dielectric substrate.

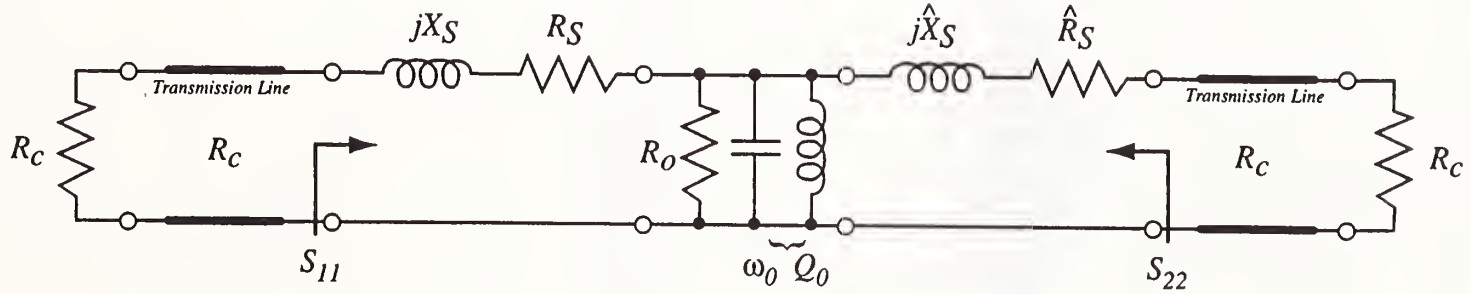

Figure 2. **Equivalent Circuit Representation of a two-port resonant cavity**

Table 1: **Measured permittivity results for Panel 1 using FSR technique.**

Measurement Mode		Frequency f_0 [MHz]	Original FSR Tech. using $f'_\ell, (\widetilde{Q}_\ell)$	Estin Model using f'_ℓ, Q'_0	Circle Fit FSR using ω_0,Q_0	Limited Circle Fit Uncert.
0	1	309.94	2.476	2.486	2.488	±0.007
1	0	439.88	2.466	2.476	2.478	±0.009
1	1	538.84	2.459	2.471	2.479	±0.017
0	2	621.92	2.474	2.477	2.478	±0.011
1	2	762.13	2.466			
2	0	881.95	2.461			
0	3	935.45	2.45			
1	3	1032.21	2.469			
2	2	1080.37	2.462			

Manufacturer's Measured Permittivity ≈ 2.47 (frequency unspecified)

Re-Entrant Cavity Measured Permittivity range 2.39 to 2.48 (at 440 MHz); ±3% uncert.)
(using old computation technique)

Table 2: **Loaded and unloaded measured quality factors for Panel 1 using FSR technique.**

Measurement Mode		Frequency f_0 [MHz]	Original FSR Tech. showing $(\widetilde{Q}_\ell)$	Estin Model showing Q'_0	Circle Fit FSR showing Q_0	Limited Circle Fit Uncert.
0	1	309.94	58.36	83.8	85.12	±2.19
1	0	439.88	65.29	92.96	95.2	±7.48
1	1	538.84	61.43	100.3	111.3	±23.45
0	2	621.92	80.02	102.5	108.8	±14.4
1	2	762.13	73.32			
2	0	881.95	81.15			
0	3	935.45	65.3			
1	3	1032.21	85.51			
2	2	1080.37	90.17			

Table 3: **Measured permittivity results for Panel 2 using FSR technique.**

Measurement Mode		Frequency f_0 [MHz]	Original FSR Tech. using $f'_\ell, (\widetilde{Q}_\ell)$	Estin Model using f'_ℓ, Q'_0	Circle Fit FSR using ω_0,Q_0	Limited Circle Fit Uncert.
0	1	234.36	4.059	4.159	4.184	±0.0606
0	1	234.38	4.064	4.173	4.196	±0.0556
1	0	333.06	4.092	4.145	4.158	±0.0805
1	1	405.66	4.001	4.149	4.185	±0.128
0	2	473.79	4.084	4.123	4.118	±0.096
1	2	578.17	4.019	4.116	4.14	±0.081

Stripped Sample Re-Entrant Cavity Measured Permittivity ≈ 4.22 (at 568 MHz; ±1% uncert.)
Open-Ended Coax Measured Permittivity ≈ 4.23 (at 580 MHz)

Table 4: **Loaded and unloaded measured quality factors for Panel 2 using FSR technique.**

Measurement Mode		Frequency f_0 [MHz]	Original FSR Tech. showing $(\widetilde{Q}_\ell)$	Estin Model showing Q'_0	Circle Fit FSR showing Q_0	Limited Circle Fit Uncert.
0	1	234.36	19.33	41.29	42.93	±4.3
0	1	234.38	19.36	42.25	44.436	±4.7
1	0	333.06	27.63	44.97	53.23	±19.1
1	1	405.66	16.24	39.85	41.06	±15
0	2	473.79	32.87	48.35	50.49	±12.03
1	2	578.17	21.55	46.88	48.386	±16.3

Table 5: **Relative-permittivity uncertainties using the FSR technique.**

Frequency and quality factor uncertainties for specific materials
are based on measurements; other uncertainties are best estimates.

(Side Length uncertainty includes fringing for the first column only.)

Uncertainty Source	Original Estimate	Panel 1 Uncertainty	Panel 2 Uncertainty
Frequency	4%	0.9%	2%
Quality Factor	1.6%	0.4%	1.2%
Side Length (fringing)	1.2%	0.4%	0.4%
Fringing Capacitance	n.a.	0.9%	2.9%
Coupling Perturbation	2%	1%	1%
Adjacent Resonances	1%	1%	1%
Combined Uncertainty	+7%,−3%	+3%,−1%	+5%,−3%

Table 6: **Measured unloaded quality factor and computed conductivity quality factor for Panel 1 using FSR technique.**

Measurement Mode		Frequency [MHz]	Computed Q_C	Circle Fit Q_0	Circle Fit $tan\,\delta + 1/Q_R$	Estin Q_0'	Estin $tan\,\delta + 1/Q_R$
0	1	309.94	101.6	85.12	0.0019	83.8	0.0021
1	0	439.88	121.0	95.2	0.0022	92.96	0.0025
1	1	538.84	133.9	111.3	0.0015	100.3	0.0025
0	2	621.92	143.9	108.8	0.0022	102.5	0.0028

Measured reentrant cavity value for $tan\,\delta \approx 0.001$.

Table 7: **Measured unloaded quality factor and computed conductivity quality factor for Panel 2 using FSR technique.**

Measurement Mode		Frequency [MHz]	Computed Q_C	Circle Fit Q_0	Circle Fit $tan\,\delta + 1/Q_R$	Estin Q_0'	Estin $tan\,\delta + 1/Q_R$
0	1	234.36	340.8	42.93	0.0204	41.29	0.0213
0	1	234.38	340.7	44.436	0.0196	42.25	0.0207
1	0	333.06	406.2	53.23	0.0163	44.97	0.0198
1	1	405.66	448.3	41.06	0.0221	39.85	0.0229
0	2	473.79	484.5	50.49	0.0177	48.35	0.0186
1	2	578.17	535.2	48.386	0.0188	46.88	0.0195

Measured reentrant cavity value for $tan\,\delta \approx 0.0185$.

Flow Chart 1. **List of main program softkey labels and their corresponding subprogram CALL statements.**

Softkey label	Subprogram call	Next call & RETURN
"NEW DATA MEASURE"	CALL Input_info	CALL Read_nwa
"DATA FIT ROUTINES"	CALL Fit_data	(see flow chart 2)
"STORE DATA"	CALL Save_results	RETURN
"READ DAT FILE"	CALL Read_file	RETURN
"STOP PROGRAM"	STOP	

Flow Chart 2. **List of subprogram CALL sequences for the main subprogram "Fit_data" called by selecting the softkey "DATA FIT ROUTINES".**

SUB Fit_data
Main driving subprogram for initiating data fit procedure, calculating total resonant cavity parameters, and carrying out an FSR permittivity calculation.

CALL Fit_circle: S_{11} data array
Carry out circle data fit for indicated data array
(see Flow Chart 3 for subprogram call sequence)

CALL Straight_line: S_{21} data array
Carry out linear data fit for indicated data array
(see Flow Chart 3 for subprogram call sequence)

CALL Fit_circle: S_{22} data array
Carry out circle data fit for indicated data array

CALL Straight_line: S_{12} data array
Carry out linear data fit for indicated data array

CALL Calc_qualty_fac
Calculate total coupling coefficient for cavity, then compute unloaded quality factor and unloaded frequency.
Repeat using values and formulation from earlier research.
(Output: κ, $\widehat{Q}_0$, $\{[\kappa_1 X_1 + \hat{\kappa}_1 \hat{X}_1]/[\widehat{Q}_0 R_c]\}$, $\{\omega_0/\omega_\ell\}$, ω_0, Q_0; κ', Q_0')

CALL Qual_fac_unct
Carry out uncertainty calculations for principal resonant cavity parameters
(Output: Alternate (κ, $\widehat{Q}_0$, $\{[\kappa_1 X_1 + \hat{\kappa}_1 \hat{X}_1]/[\widehat{Q}_0 R_c]\}$, $\{\omega_0/\omega_\ell\}$, ω_0, Q_0) ;
Uncertainty [κ, ω_0, Q_0])

CALL Fsr_permittivty
Calculate FSR permittivity using previously obtained principal resonant cavity parameters.
Repeat using earlier research formulation's values.
(Output: ϵ_r', $\epsilon_{r_{(est)}}'$) ; Uncertainty $[\epsilon_r']$

CALL Display_results
Display results from the above calculations.

Flow Chart 3. **List of subprogram CALL sequences for the principal least-squares data fitting subprograms.**